Electroactive γ-phase, enhanced thermal and mechanical behaviour and high ionic conductivity response of poly(vinylidene fluoride) / cellulose nanocrystals hybrid nanocomposites

E. Lizundia[1,2,], A. Reizabal[2], C. M. Costa[3,4,*], A. Maceiras[2], S. Lanceros-Méndez[2,5]*

[1]Department of Graphic Design and Engineering Projects, Bilbao Faculty of Engineering, University of the Basque Country (UPV/EHU), Bilbao 48013, Spain.

[2]BCMaterials, Basque Center Centre for Materials, Applications and Nanostructures, UPV/EHU Science Park, 48940 Leioa, Spain.

[3]Centro de Física, Universidade do Minho, 4710-057 Braga, Portugal

[4]Centro de Química, Universidade do Minho, 4710-057 Braga, Portugal

[5]IKERBASQUE, Basque Foundation for Science, 48013 Bilbao, Spain

[*]**Corresponding Authors E-mail:** E. Lizundia (erlantz.liizundia@ehu.eus); C.M. Costa (cmscosta@fisica.uminho.pt)

Abstract

Cellulose nanocrystals (CNCs) are incorporated into poly (vinylidene fluoride) (PVDF) to tailor the mechanical and dielectric properties of this electroactive polymer. PVDF/CNC nanocomposites with concentrations up to 15 wt% have been prepared by solvent-casting followed by quick vacuum drying in order to ensure the formation of the electroactive γ-phase. The changes induced by the presence of CNCs on the morphology, crystalline structure, thermal properties, mechanical performance and dielectric behaviour are explored. Results suggest a relevant role of the CNC surface –OH groups which interact with PVDF fluorine atoms. The real dielectric constant ε' of nanocomposites at 200 Hz increases by 3.6 times up to 47 for the 15 wt.% CNC nanocomposite due to an enhanced ionic conductivity provided by CNCs. The approach here reported in order to boost the formation of the γ-phase of PVDF upon the incorporation of CNCs serves to further develop cellulose-based multifunctional materials.

Keywords: A. Cellulose; A. Nanocomposites; B. Electrical properties; B. Mechanical properties.

1. Introduction

Poly (vinylidene fluoride) (PVDF) is a thermoplastic fluoropolymer with large potential in the fields of sensing, actuation, energy storage and harvesting systems and drug delivery, mainly thanks to its electroactive properties (ferro, pyro and piezoelectric) [1,2][3,4]. This semicrystalline polymer could be found in five different polymorphs (*α, β, γ, δ* and *ε*), being the *α*-phase it's most common polymorph. Traditionally, *β*-phase PVDF has represented the most technologically relevant phase as it provides a net dipole moment and the largest piezoelectric response among polymers, making PVDF useful for many multifunctional applications [5]. Thus, the development of *β*-phase PVDF has been intensively pursued in recent years [2]. As melt-processing usually yields *α*-phase, PVDF films comprising *β*-phase are commonly obtained upon stretching *α*-phase [6]. Other techniques have been reported so far to effectively promote the formation of such *β*-phase, including annealing [7], poling (a preferred orientation of the dipoles along the field direction is induced) [8], and filler addition [9,10].

Interestingly, the *γ* phase of PVDF is another polar and electrically active phase of PVDF that has been less used for applications [11]. This phase has been typically obtained through the solid-state phase transformation (α-γ) at temperatures close to melt temperature or upon the addition of different fillers such as clays [12]. Filler addition represents a versatile approach to trigger the different crystalline phases of PVDF as it usually also encompasses the improvement of mechanical, thermal and electrical properties of the matrix. Moreover, no extensive use of equipment is required since fillers can be directly incorporated during the fabrication process, resulting in a cost and time effective approach [2].

In this framework, the addition of fillers such as carbon nanotubes (CNT) [13], barium titanate ($BaTiO_3$) [14], or montmorillonites within PVDF matrix has been proved to be an efficient approach to enhance the piezoresponse behaviour of PVDF [15]. Therefore, a suitable approach to develop PVDF-based materials with improved functionalities may be the introduction of novel organic materials that acting as nucleating agents could lead to specific crystalline phases. Cellulose nanocrystals (CNCs) result attractive candidates as they have been proven to prompt the crystallization process of many semicrystalline polymers [16–19]. CNCs are crystalline rod-shaped nanoparticles that can be obtained upon the controlled cleavage of the amorphous regions of cellulose [20]. These nanoparticles which can be disintegrated

under composting conditions [21], present a high Young´s modulus of 130 GPa [22], and can be synthesized from any cellulose source material using mechanical, chemical or enzymatic approaches [20]. The large abundance of cellulose, its mechanical stability at relatively high temperatures [23], low cost and non-toxicity make CNCs interesting reinforcing elements to improve the piezoelectric properties of PVDF while lowering the environmental burden associated with the use of traditional plastics [24,25].

Apart from being renewable, wood is known to present the piezoelectric effect [26], although its highly heterogeneous non-crystalline structure usually results in a relatively small piezoelectric constant. In contrast to wood, CNCs present a highly crystalline structure. Since asymmetric crystalline structures have been proven to show piezoelectric response, the development of such highly crystalline particles makes CNCs by themselves an electroactive material with interesting electroactive properties [27]. The high-aspect ratio of CNCs may help to induce the different conformations to PVDF as the provided large surface-area could serve as heterogeneous nucleation sites of PVDF [28], while the large amount of available –OH groups on the surface of CNCs may interact with PVDF fluorine atoms to yield a net dipolar moment.

Although several works have reported on the preparation of PVDF/cellulose blends [29–31], none of them has focus on the effective nucleation of the electroactive phases of PVDF using CNCs. Therefore, here CNCs have been introduced with different contents up to 15 wt% into PVDF in order to induce morphological changes and nucleate electroactive phases of PVDF due to available –OH groups on the surface of CNCs. The influence of CNC incorporation into PVDF on the morphology, thermal stability and mechanical performance is also investigated and these nanocomposites can be used in new applications considering natural reinforcements based on wood.

2. Materials and Methods

2.1. Starting materials

Microcrystalline cellulose (310697-500G), sulphuric acid and dimethylformamide (DMF) were obtained from Sigma Aldrich, while poly (vinylidenefluoride) (PVDF) with a molecular weight of M_w = 300 kg·mol^{-1} was purchased from Solvay (Solef 6010).

2.2. CNCs synthesis and their transfer from water to DMF

Cellulose nanocrystals (CNCs) are extracted by a controlled chemically-induced cleavage of cellulose via strong acid hydrolysis. Different acids including hydrochloric, nitric, hydrobromic and phosphoric acids can be used, although sulfuric-acid induced extraction is the most commonly found method [32–34]. Accordingly, CNCs were synthesized by sulphuric acid hydrolysis approach. CNCs were obtained by hydrolyzing microcrystalline cellulose with a 64% (w/w) sulphuric acid solution at 45 ºC for 30 min under vigorous magnetic stirring [19]. The reaction was quenched by adding 10-fold distilled water and the resulting suspension was centrifuged several times at 4000 rpm for 15 min to concentrate the remaining cellulose and to remove excess aqueous acid. Nanosized cellulose was obtained after sonication (Vibracell Sonicator, Sonics and Materials Inc., Danbury, CT) at 50% output for 15 min. The suspension was dialyzed for 7 days using Visking dialysis membranes (molecular weight cut off from 12.000 to 14.000 Da; Medicell Membranes Ltd). Water-dispersed CNCs were exchanged to DMF through centrifugation using acetone as intermediate solvent (each step comprised centrifugation at 4000 rpm for 15 min). DMF-dispersed CNCs where stored at 4 ºC.

2.3. Nanocomposite fabrication

PVDF/CNC nanocomposite films at a 1, 5, 10 and 15 wt.% were obtained through solvent-casting followed by quick vacuum drying. After dissolving PVDF in DMF, the required amount of CNC was added to obtain 14 % (by weight) dispersions. After dispersion by magnetic stirring plate (Ika, model no. C-MAG HS 7) and sonication (Vibracell Sonicator, Sonicsand Materials Inc., Danbury, CT), the mixtures were cast onto Petri-dishes and the DMF was rapidly removed by vapor chamber under vacuum (JPSelecta Vacuo-Temp) at 70 ºC [2,35]. For comparison, we also fabricated films upon slow evaporation of DMF at 60 ºC at atmospheric pressure (see Fig. S1 for its morphological, conformational, thermal and mechanical properties).

2.4. Characterization

CNC morphology was evaluated by transmission electron microscopy (TEM) using a Philips CM120 Biofilter apparatus with STEM module (120 kV). A droplet of a 0.1% (w/w) water-dispersed CNCs was deposited onto a carbon-coated grid and then samples were negatively stained with 1% uranyl acetate during 1 min. PVDF/CNC nanocomposite morphology was examined using a scanning electron microscope (SEM, NanoSEM - FEI Nova 200 (FEG/SEM)) at an accelerating voltage of 15 kV. Before analysis, samples were coated with a gold layer by sputtering with a Polaron SC502 apparatus.

Attenuated total reflectance Fourier transform infrared spectroscopy (ATR-FTIR) of CNCs was performed on a Bruker Alpha FT-IR Spectrometer equipped with diamond ATR optics. The occurrence of any interaction between CNCs and hosting PVDF was evaluated with a Jasco FT/IR-4100 system. FTIR spectra were obtained from 4000 to 600 cm^{-1} after 64 scans with a resolution of 4 cm^{-1}.

The X-ray powder diffraction (XRD) patterns were recorded on a PANalytical Empyrean diffractometer in reflection mode using Cu Kα radiation (λ = 1.5418 Å) and operating at 45 kV and 40 mA.

Thermal transitions were analyzed by differential scanning calorimetry (DSC), while thermal stability was investigated through thermogravimetric analysis (TGA). DSC was carried by Netzsch DSC 204 F1 Phoenix instrument under a flowing nitrogen atmosphere between 25 and 200 ºC at a rate of 10 $ºC \cdot min^{-1}$ (for both cooling and heating). All samples were measured in 40 µL aluminium pans with perforated lids. TGA was performed in a TGA Q500 (TA Instruments) between 30 at 700 ºC at $20ºC \cdot min^{-1}$ under a N_2 flow of 50 $mL \cdot min^{-1}$.

Mechanical behavior of PVDF nanocomposites was evaluated under tensile testing using an Autograph AGS-J from Shimadzu. Samples were conditioned at 22 ºC and 51 % relative humidity overnight before testing. Stress-strain curves were obtained at a 5 $mm \cdot min^{-1}$ for 5 mm width, 12 mm height (l_0) and 0.05 mm thick samples. The Young's modulus (*E*) value for each sample was obtained from the slope in stress-strain curve within the initial linear elastic region, i.e. from the slope between 0.5 – 1.5 % strain ($\Delta l/l_0$) in the stress-strain curves. All tests were performed according to the ASTM D882 standard for sample thickness below 1 mm (reported values were determined as the mean value of 5 samples).

Dielectric measurements at room temperature were carried out with a Quadtech 1920 LCR precision in the 20 Hz - 1 MHz frequency range with an applied voltage of 0.5 V. 5 mm diameter aluminum electrodes were vacuum evaporated onto both sides of each sample. The error associated to the dielectric measurements is about 2%. The real part of the dielectric function (ε'), the dielectric losses ($tan\ \delta$) and real part of the conductivity function (σ') were obtained according to:

$$\varepsilon' = \frac{C.d}{\varepsilon_0.A}, \quad (1)$$

$$\tan\delta = \frac{\varepsilon''}{\varepsilon'}, \quad (2)$$

$$\sigma' = \varepsilon_0 \omega \varepsilon'', \quad (3)$$

where A indicates the plate area, d is a plate distance, ε_0 ($8.85x10^{-12}$ $F{\cdot}m^{-1}$) is the permittivity of free space, $\varepsilon' and\ \varepsilon''$ are the real and imaginary dielectric constant respectively and $\omega=2\pi\nu$ is the angular frequency.

3. Results and discussion

3.1. CNC characterization

Here we develop PVDF/CNC nanocomposites through solvent casting and vacuum fast drying in order to induce the nucleation of the γ-phase of PVDF towards enhanced electroactive properties. Synthesized CNCs present a rod-shaped morphology with a length of 135 ± 21 nm and a width of 7 ± 1 nm in width (see Fig. 1a). FTIR and XRD results show the characteristic features for cellulose I, with a wide band in the 3650-3200 cm^{-1} region and narrower bands in the 1500-800 cm^{-1} region of the FTIR spectrum and three main diffraction peaks at 2θ = 14.7º, 16.4º and 22.7º respectively in the XRD pattern [36–39]. As a result of the sulphuric acid assisted hydrolysis, CNC surfaces are decorated with sulphate half-ester groups, yielding negatively charged surfaces with an average zeta potential (ζ-potential) values of – 39.6 ± 0.9 mV (pH = 2.3, 0.1 $mg{\cdot}mL^{-1}$ aqueous solution at 25 °C). Further evidence of the sulphate half-ester groups is observed in the FTIR absorption band located at 1033 cm^{-1} (see Fig. S2). Such negatively charged character of CNC surfaces may serve to induce an electroactive phase nucleation in PVDF as positively charged CH_2 groups within PVDF interact with sulphate half-ester groups onto CNCs to yield an extended TTTT conformation [1,10]. This TTTT conformation corresponds to the all-trans conformation of PVDF and is

formed due to the fact that CNC surfaces promote crystallization of the PVDF chains into all-trans conformation through the interaction of sulphate half-ester groups with the dipole moments of PVDF.

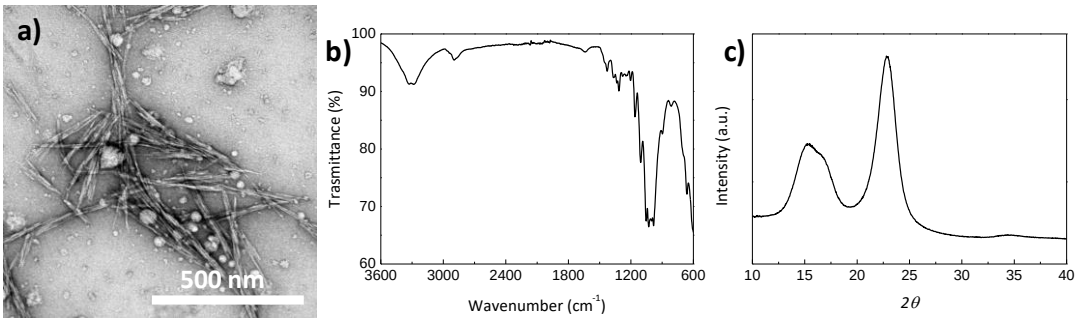

Fig. 1. (a) Representative transmission electron microscopy (TEM); (b) FTIR spectrum and (c) XRD pattern of CNCs.

3.2. Morphology and structure of PVDF/CNC nanocomposites

PVDF/CNC nanocomposite morphology was firstly assessed by scanning electron microscopy (SEM) as it could provide insights on the morphology of PVDF and the degree of CNC dispersion [9]. Fig. 2 shows SEM micrographs of cryogenically fractured PVDF (a, c) and PVDF/CNC (b, d) surfaces. As observed in both low and high magnification SEM images (Fig. 2a and 2c), neat PVDF presents a relatively smooth fracture surface with some scattered spherulites [9,28]. This morphology markedly differs from the one obtained upon drying at 60 °C under atmospheric pressure (Fig. S1a), which fails to provide the electroactive γ-phase. Upon CNC addition the fracture surface becomes notably rougher, suggesting that the presence of CNCs prompts PVDF crystallization (this fact is quantitatively shown in Table 1). Additionally, no traces of CNC bundles could be observed in the high-magnification SEM image in Fig. 2d, suggesting a good physical compatibility of CNCs within the polymeric matrix without cracks and agglomerates [40].

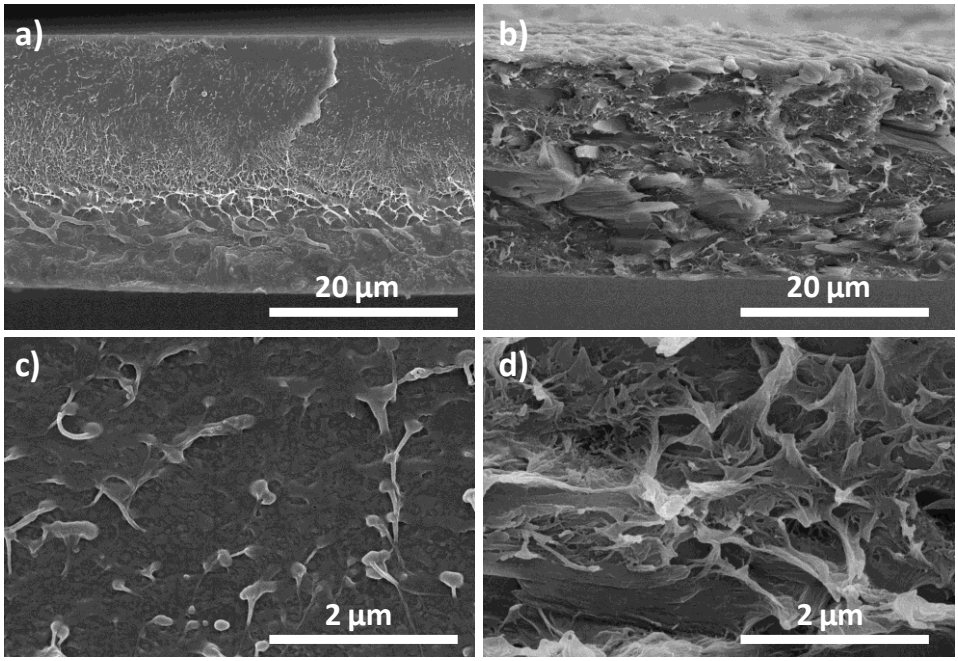

Fig. 2. SEM micrographs of cryogenically fractured PVDF (a and c at higher magnification) and PVDF/CNC 10 wt.% nanocomposite surfaces (b and d at higher magnification).

The occurrence of different phases in PVDF nanocomposites can be studied by X-ray diffraction and Fourier transform infrared spectroscopy (FTIR). Accordingly, Fig. 3 presents wide angle X-ray diffraction (WAXD) patterns and FTIR spectra for PVDF/CNC nanocomposites with CNC concentrations up to 10 wt%. The three peaks located at 2θ = 14.9°, 16.5° and 22.7° correspond to *(1-10)*, *(101)* and *(200)* planes of cellulose I phase [38,41]. PVDF and PVDF/CNC nanocomposites display three peaks located at 18.7°, 20.4° and ~27°, which correspond to *(020)*, *(110)* and *(021)* planes that are characteristic of the γ-phase [12].

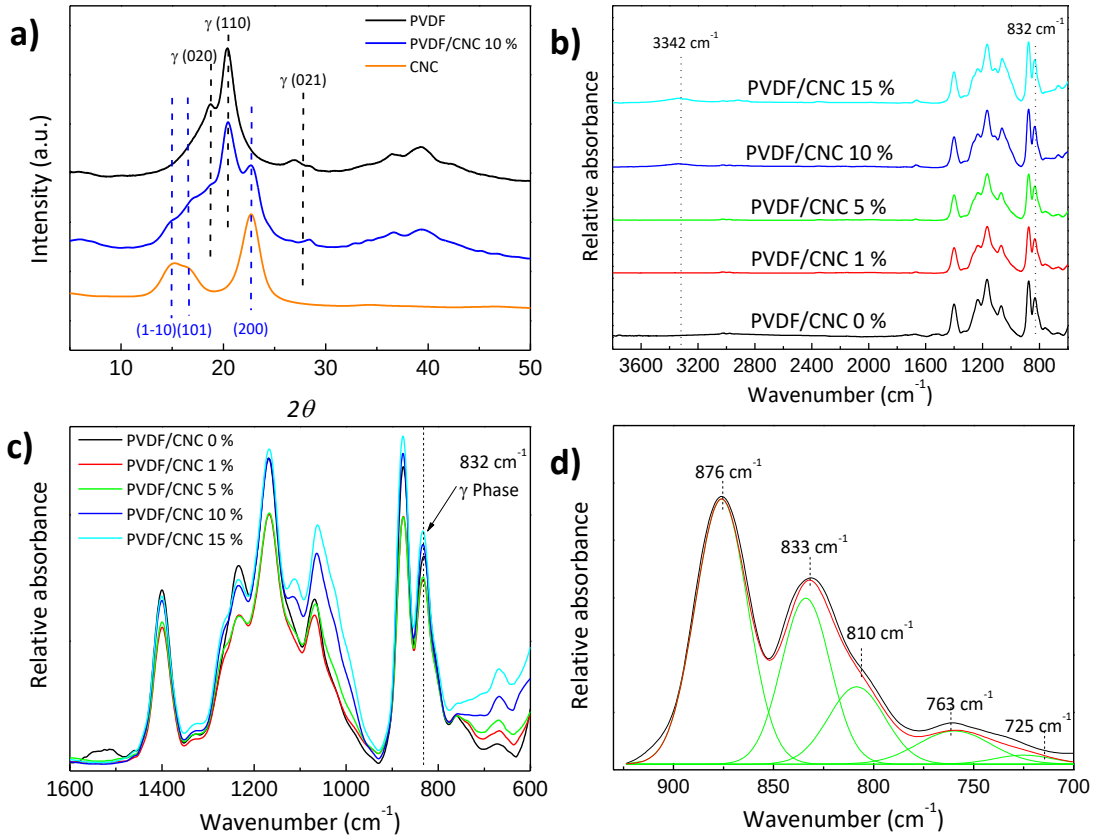

Fig. 3. (a) WAXD patterns; (b) FTIR spectra and (c) enlarged FTIR spectra of PVDF/CNC nanocomposites. (d) Peak deconvolution for PVDF.

The presence of the γ-phase of PVDF is also confirmed through the FTIR spectra in Fig. 3b to 3d (see Fig. S1b for the FTIR spectrum of the film dried at 60 °C under atmospheric pressure). For neat PVDF, the specific characteristic bands are 766, 796, 855 and 976 cm^{-1} for α-PVDF, 840 and 1275 cm^{-1} for β-PVDF and 812, 833, 838 and 1234 cm^{-1} for γ-PVDF. Although it is difficult distinguish the peaks related to β-phase and γ-phase in the 800 to 900 cm^{-1} region, the specific bands corresponding to the γ phase could be observed at 431, 812 and 1234 cm^{-1} [42]. The specific band characteristics of α-phase at 766 cm^{-1} and γ-phase at 812 and 833 cm^{-1} are identified in the Fig. 3b and 3c for all PVDF/CNC nanocomposites, while Fig. 3d shows the peak deconvolution for the PVDF (the specific bands for α and γ-phases are highlighted). As shown in Fig. 3c, the obtained spectra do not change with the CNC concentration. Therefore, we estimate that the main reason for γ-phase nucleation results the vacuum application during sample preparation, where the solvent evaporates fast to yield γ-phase. Typically, in the conventional oven at temperatures below 90 ºC, the evaporation rate is low, i.e. the lower polymer-chain mobility leads to crystallization in the β-phase.

On the contrary, upon vacuum application, the polymer is able to crystallize into the other electroactive γ-phase. Further, it is to notice that this effect is independent of the filler content and, therefore, sample processing conditions are more determinant on phase content that the presence of the filler.

In order to quantify this effect, the crystalline phase content the two specific bands at 766 cm^{-1} and 833 cm^{-1} that represent the α- and γ-phases respectively and the method explained elsewhere were used [12]:

$$F(\gamma) = \frac{X_\gamma}{X_\alpha + X_\gamma} = \frac{A_\gamma}{(K_\gamma/K_\alpha)A_\alpha + A_\gamma}, \quad (4)$$

where, A_α and A_γ represent the absorbencies at 766 and 833 cm^{-1} corresponding to α- and γ-phases, K_α and K_γ are the absorption coefficients at the respective wavenumbers (set at 0.365 and 0.150 μm^{-1} respectively) and X_α and X_γ represent the degree of crystallinity of each phase. The amount of γ-phase remains at ~90 % for all the compositions, including pristine PVDF, confirming the previous discussion.

3.3. PVDF/CNC thermal and mechanical properties

Differential scanning calorimetry (DSC) was performed to study the occurrence of thermal transitions in PVDF/CNC nanocomposites. Fig. 4a shows the first DSC heating scans of PVDF/CNC films obtained at a heating rate of 10 °C·min^{-1} (see Fig. S1c for the DSC scan corresponding to the film dried at 60 °C under atmospheric pressure). A sharp endothermic peak is observed at a temperature of nearly 173 °C (identified as T_m melting temperature), which is due to the melting of the crystalline domains within the material [1]. It is observed that CNC incorporation leads to a slight decrease of the T_m of the nanocomposites from 172.5 ºC for neat PVDF up to a minimum of 171.3 ºC for the 15 % nanocomposite. This effect is related to the fact that CNCs act as nucleating elements, resulting in the formation of extra but smaller and slightly more imperfect crystals when compared to neat PVDF [43]. Interestingly, the heat capacity change (ΔC_p) at T_g is markedly reduced upon the addition of CNCs. This effect that arises from the constraining behaviour of CNC surfaces on the mobility of the amorphous regions of PVDF is a typically found behaviour in polymer nanocomposites and is often referred as chain confinement [44,45]. As an increase in CNC concentration is accompanied by a rise on the amount of CNC surfaces available to interact with PVDF

chains, samples containing larger concentrations of CNCs present a less marked ΔC_p. The addition of CNCs does not substantially modify the melting temperature of the nanocomposites at it remains at 172 ± 1 ºC for all the compositions. We use the extent of the melting endotherm to quantitatively determine the crystalline fraction X_c (%) of prepared nanocomposites as:

$$X_c(\%) = \frac{\Delta H_f}{\Delta H_f^0 \cdot W_m}, \quad (5)$$

where ΔH_f is the fusion enthalpy measured during the heating scan, W_m is the PVDF matrix weight fraction and ΔH_f^0 is the heat of fusion of an infinitely thick PVDF crystal (set at 104.6 $J \cdot g^{-1}$) [1]. The crystalline fraction present in PVDF/CNC nanocomposites is shown in Table 1. It can be observed that the crystalline fraction is affected by the amount of CNCs present in the nanocomposite. In fact, all nanocomposites show an increasing crystalline fraction independently of the CNC concentrations when compared to the neat PVDF and the highest crystalline fraction was obtained for nanocomposite with 1% by weight. The main reason is due to the fact that CNCs are effective nucleating agents for PVDF crystallization [19,40]. At concentrations exceeding 5%, on the contrary, the X_c increase upon CNC incorporation (in comparison with neat PVDF) is less pronounced due to the competing nucleating and constraining behavior of CNC surfaces originated by aggregated CNC crystals. In other words, although CNC surfaces can effectively nucleate CNC crystallization, large CNC fractions do not allow polymer chains to pack into ordered large structures [19,40], yielding smaller X_c increase.

Table 1. X_c crystalline fraction for PVDF/CNC nanocomposites.

Sample name	**X_c (%)**
PVDF/CNC 0%	38 ± 2
PVDF/CNC 1%	53 ± 4
PVDF/CNC 5%	48 ± 2
PVDF/CNC 10%	43 ± 2
PVDF/CNC 15%	48 ± 3

The study of the thermally-induced degradation in thermoplastics is of paramount relevance towards the applicability of the developed materials as the onset of the

thermal degradation determines both the maximum processing temperature during conformation processes and the upper limit to service temperature. In this sense, thermogravimetric analysis (TGA) in N_2 atmosphere was carried out for PVDF/CNC films. Fig. 4b shows the TGA curves (left axis, solid line) and weight loss rates or DTGA curves (right axis, dotted line) of the PVDF/CNC nanocomposites. A marked effect on the thermodegradation behaviour of PVDF is observed after CNC incorporation. While the thermal degradation or PVDF proceeds in a single step centred at 474 °C involving the formation of fragments arising from vinylidene monomers, dimers and oligomers [46], CNC incorporation progressively yields a new thermodegradation process at temperatures of 243 °C. This process, which is easily observed as a step on the TGA curves and as a peak on the DTGA curves, comprises the degradation of less-thermally stable CNC fraction within the nanocomposites as a result of depolymerization, dehydration and decomposition of cellulosic glycosyl units [47]. In any case, it should be noted that the temperature at which the maximum degradation rate is obtained, T_{peak}, remains barely unchanged at ~474 °C, suggesting that the presence of CNCs does not catalyze thermodegradation reactions in PVDF.

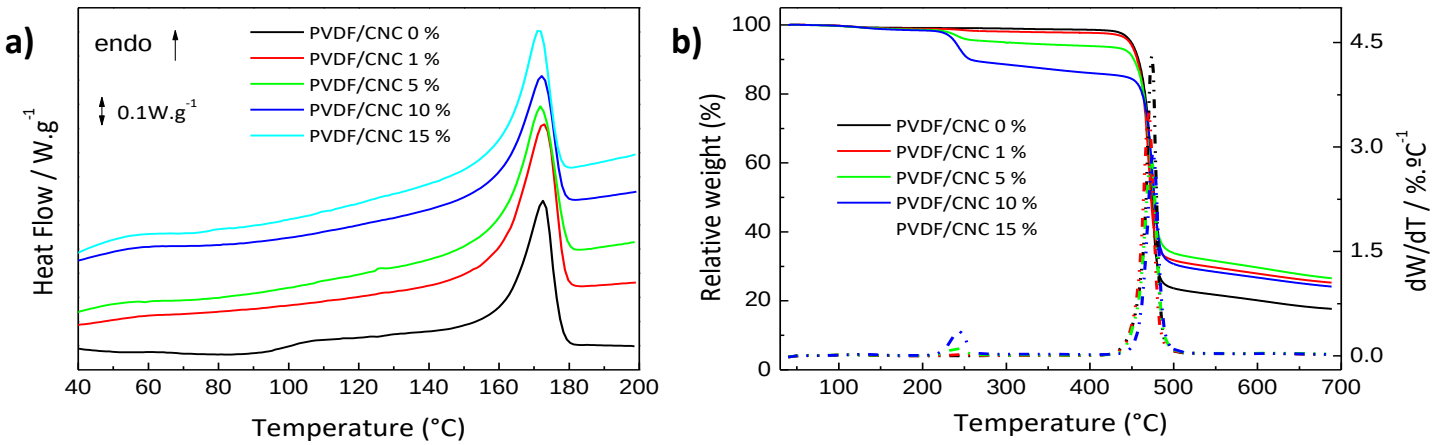

Fig. 4. (a) DSC heating curves and (b) TGA traces of PVDF/CNC nanocomposites.

Mechanical properties of nanocomposites were evaluated by uniaxial tensile testing. Representative stress-strain curves of PVDF/CNC nanocomposites are shown in Fig. 5. Neat PVDF has a ductile behaviour with a stress at yield (σ_y) of 39.6 MPa, strain at yield (σ_y) of 6.8 % and strain at break (ε_b) of about 250 %, matching well with previously reported data and in contrast with the brittle behaviour of neat PVDF when dried at 60 °C under atmospheric pressure (see Fig. S1d for the corresponding tensile

stress-strain curve) [9]. The incorporation of CNCs is accompanied by a dramatic reduction in ε_b up to values as low as 4.5 % for its 15 wt.% nanocomposite as similarly found in other CNC-reinforced polymeric systems [40,48]. This is a commonly found effect in polymer nanocomposites and is ascribed to a poor interfacial adhesion between the filler and the matrix, yielding inefficient local stress transference [49,50]. This continuous embrittlement upon CNC incorporation is accompanied by a marked increase in both Young´s modulus ($E´$) from 1035 ± 170 MPa for neat PVDF to 1662 ± 47 MPa for its 15% nanocomposite counterpart. In any case, it is worthy to note that at low concentrations, i.e. 1 and 5%, CNC incorporation notably decreases both E and σ_y up to a minimum of 427 ± 63 MPa and 14.3 MPa respectively, indicating a poor interfacial compatibility between the hydrophobic character of PVDF and the highly hydrophilic CNCs [51,52]. The fact that the Young´s modulus markedly increases at high loadings can be ascribed to the formation of a stiff interconnected CNC network, which is able to resist the uniaxial stretching [53]. It is also noticed that although the E modulus increases upon CNC addition caused by the increases the chain rigidity, tensile strength slightly decreases at a concentration of 15% CNC. This effect arises from the weak interfacial compatibility between CNC and PVDF, which effectively transfer stresses at low strains (therefore, E increases) but fail to effectively reinforce the whole system at high strains [54]. Overall, the interfacial compatibility could be improved by surface grafting of CNCs before their introduction into the PVDF as the grafted chains could create a co-continuous phase for the efficient transfer of local stresses within the bulk material [55].

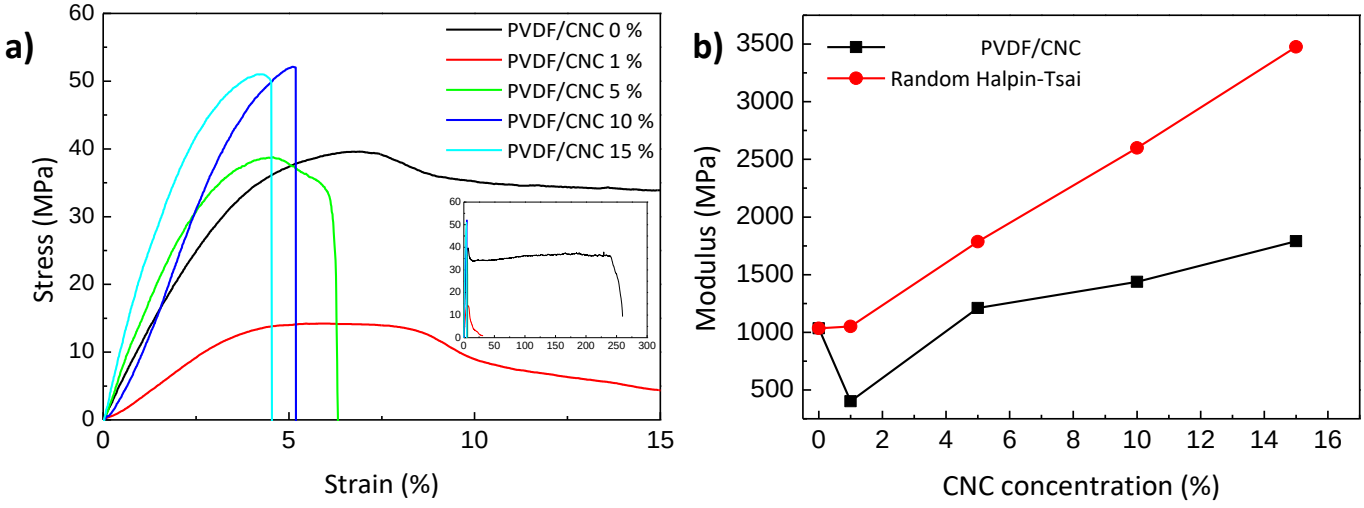

Fig. 5. (a) Stress-strain tensile curves of PVDF/CNC nanocomposites and (b) experimental data and fitting results according to the modified Halpin-Tsai model.

Experimental results can be compared with theoretical predictions according to the modified Halpin-Tsai model [56]:

$$\frac{E_c}{E_m} = \left(\frac{3}{8}\right)\left(\frac{1+2\rho\eta_L V_{CNC}}{1-\eta_L V_{CNC}}\right) + \left(\frac{5}{8}\right)\left(\frac{1+2\eta_T V_{CNC}}{1-\eta_T V_{CNC}}\right), \quad (6)$$

$$\eta_L = \frac{E_r - 1}{E_r + 2\rho} \qquad \eta_T = \frac{E_r - 1}{E_r + 2}, \quad (7)$$

where E_c and E_m is the Young´s modulus of the nanocomposite and PVDF matrix respectively, ρ is the CNC aspect ratio, V_{CNC} is its volume fraction and E_R is the ratio between the Young´s modulus of CNCs ad the PVDF matrix. CNC volume fractions are calculated from the weight fraction and densities of PVDF and CNC (1.78 g·cm^{-3} for PVDF and 1.6 g·cm^{-3} for CNC [57]), while the Young's modulus of CNCs is computed as 105 GPa [58]. The comparison between predicted and experimentally obtained *E* values according to Eq. 6 is shown in Fig. 5b. It is observed that the experimental values remain below the predicted *E* for all the studied compositions. This effective modulus of elasticity overprediction, especially for 1 wt% concentration, indicates an ineffective stress transfer across the PVDF-CNC interfaces [40,45]. Interestingly, at very low concentrations PVDF-CNC interfaces are weak points where concentration stresses are formed upon uxiaxial stretching, yielding to a marked decrease of *E*. As CNC concentration increases, the formation of a percolated three-dimensional (3D) cellulosic network can compensate the effect caused by weak PVDF-CNC interfaces to yield increased *E* values.

3.4. PVDF/CNC dielectric properties

Dielectric spectroscopy was conducted to understand the effect of CNC incorporation on the dielectric response of PVDF/CNC nanocomposites. Fig. 6a reports the influence of the CNC concentration on the real part of the permittivity in the 10^2-10^6 range Hz, while the dielectric loss tangent ($tan\ \delta = \varepsilon''/\varepsilon'$) for PVDF/CNC nanocomposites is displayed in Fig. 6b. For the sake of comparison, Fig. 6c shows the real dielectric constant and the dielectric loss tangent at room temperature of the PVDF/CNC nanocomposites at 200 Hz as a function of CNC concentration. It is observed that the

dielectric constant (ε') decreases with increasing frequency due to the slower dynamic of the dipoles with respect to the applied electric field [59]. Neat PVDF film presents a dielectric constant (ε') of 13 at 200 Hz, while CNC incorporation markedly increases the ε' of nanocomposites, in particular at low frequencies. For instance, at 200 Hz, ε' increases by 3.6 times up to 47 for the 15 wt.% CNC nanocomposite. These results suggest that CNCs are able to increase the dielectric response through Maxwell-Wagner-Sillars interfacial polarization contributions and local ionic conductivity in PVDF nanocomposites [60]. This increase is notably larger than that reported for PVDF/carbon nanofibres [9], highlighting the efficiency of CNCs as additives to tune the functional properties of PVDF. For instance, high-dielectric constant polymeric membranes with high ionic conductivity may be potentially used as lithium ion battery (LIB) separators due to both enhanced ionic conductivity and increased charge carrier concentration [61]. For a given frequency, the dielectric loss tangent increases with CNC concentration, indicating the more presence of interfacial polarization and electronic dipole polarization leading to significant energy dissipation [62,63]. Similarly, the fact that the AC conductivity (σ) shown in Fig. 6d increases with both CNC loading and frequency may be explained in terms of shorter distance between the carriers upon CNC incorporation which enables charge flow via hopping mechanism [64]. Similar results have also been reported after the incorporation of cellulose nanofibers and cyanoethylcellulose into PVDF [61].

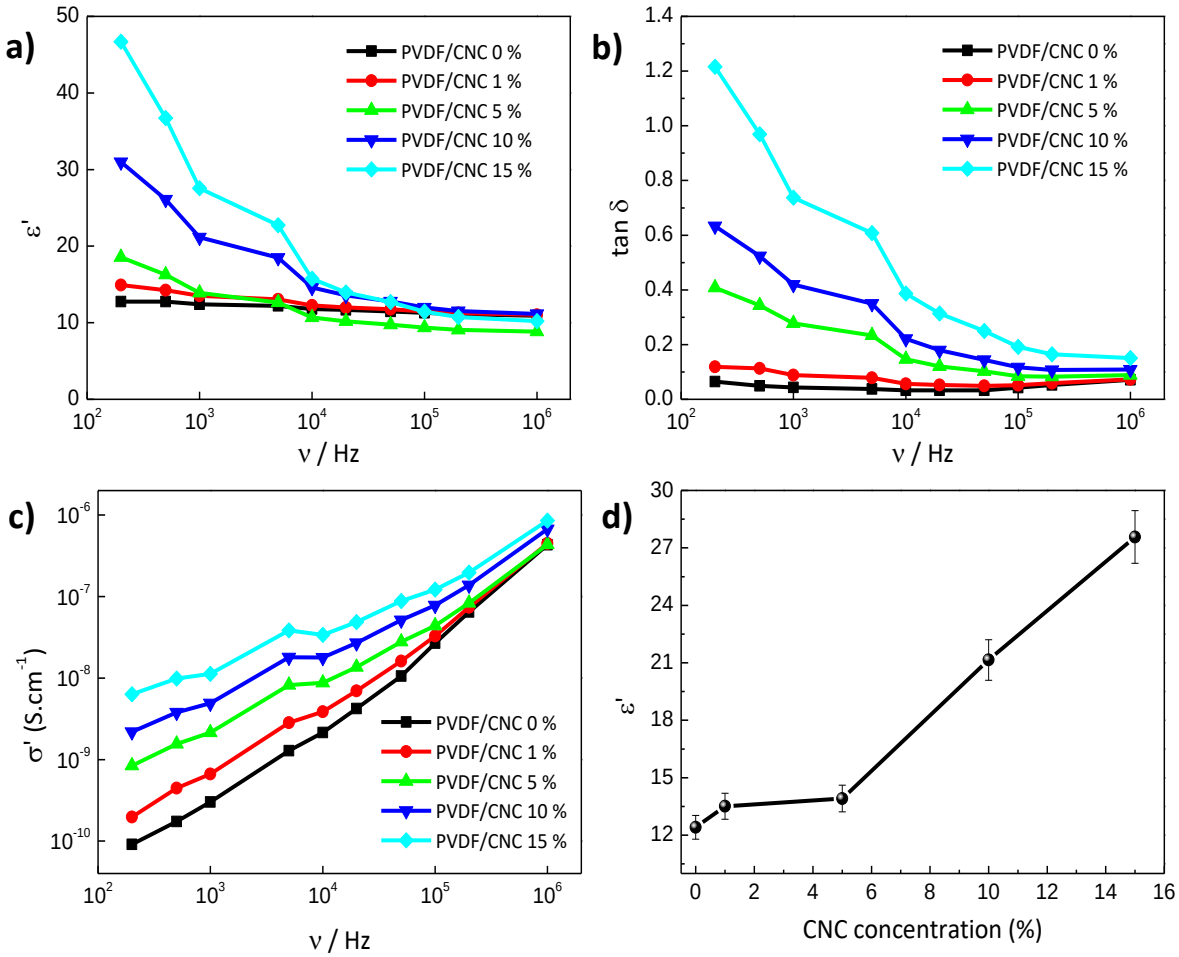

Fig. 6. Dielectric spectroscopy results: (a) Frequency dependence of the real part of the permittivity; (b) tangent loss; (c) real part of the dielectric constant and dielectric loss tangent at 1 KHz as a function of CNC concentration and (c) frequency dependence of the conductivity of PVDF/CNC nanocomposites.

The AC conductivity behaviour shown in Fig. 6d relates to the hopping transport of localized charge carriers, which can increase with CNC presence as described by [65]:

$$\sigma'(\omega) \propto \omega^n, n \leq 1\ , \tag{8}$$

where ω is the angular frequency and n ranges between $0 < n < 1$, characterizing the hopping conduction and representing the degree of the interaction between the mobile ions and the surrounded environment [66]. The n exponent extracted from the slope through Eq. 7 and Fig. 6c for all PVDF/CNC nanocomposites is shown in Table 2.

Table 2. *n* exponent for all PVDF/CNC nanocomposites.

Samples	n
PVDF/CNC 0%	0.5
PVDF/CNC 1%	0.6
PVDF/CNC 5%	0.7
PVDF/CNC 10%	0.9
PVDF/CNC 15%	1

It is observed that *n* values ranged between 0.5 to 1 and increases with CNC concentration due to the presence of negatively charged CNCs which are able to increase charge carriers in localized states and the excitation of charge carriers to upper states in the conduction band [67].

Conclusions

This work reports on the fabrication of nanocomposite materials based on PVDF and CNCs. XRD and FTIR results reveal the formation of the polar and electrically active γ-phase of PVDF for all the compositions, while high-magnification SEM observations show no traces of CNC bundles, implying a good physical compatibilization of CNCs within the polymeric matrix. It is found that the X_c crystalline fraction in PVDF increases at low CNC concentrations, yielding materials with larger electroactive γ-phase. This effect is attributed to the preparation conditions, mainly vacuum drying. The Young´s modulus of nanocomposites first decays at low concentrations to further increase from 1035 MPa for neat PVDF to 1790 MPa for its 15% nanocomposite. This behaviour is ascribed to a dual effect of poor interfacial compatibility between the hydrophobic character of PVDF and the highly hydrophilic CNCs and the formation of a percolated 3D CNC structure at high concentrations which counteract the poor interfacial compatibility to yield increased *E* values.

Dielectric spectroscopy shows a marked increase on the real dielectric constant of nanocomposites due to an enhanced ionic conductivity and charge carrier concentration provided by CNCs. Moreover, AC conductivity increases with CNC loading due to the

shorter distance between the carriers upon CNC incorporation which enables charge flow via hopping mechanism. Overall, this work provides novel pathways for the development of γ phase PVDF with high dielectric constant and improved ionic conductivity, shows a large potential to develop cellulose-based electroactive materials for multifunctional applications.

Data availability

All the data used to support the findings of this study are included within the article.

Conflicts of interest

The authors declare no competing financial interest.

Acknowledgements

The authors gratefully thank the FCT (Fundação para a Ciência e Tecnologia) for financial support under the framework of Strategic Funding grants UID/FIS/04650/2019, UID/EEA/04436/2013 and UID/QUI/0686/2016; and project no. POCI-01-0145-FEDER-028157. The authors also thank the FCT for financial support under grants SFRH/BPD/112547/2015 (C.M.C.). Financial support from the Basque Government under the ELKARTEK, HAZITEK and PIBA (PIBA-2018-06) programs is also acknowledged. Technical and human support provided by SGIker (UPV/EHU, MICINN, GV/EJ, EGEF and ESF) is gratefully acknowledged.

Appendix A. Supplementary data

Morphological, conformational, thermal and mechanical characterization of a PVDF film obtained upon drying at 60 °C at atmospheric pressure and a FTIR spectrum of synthesized CNCs. Supplementary data associated with this article can be found in the online version at doi: X.

References

[1] P. Martins, A.C. Lopes, S. Lanceros-Mendez, Electroactive phases of poly(vinylidene fluoride): Determination, processing and applications, Prog. Polym. Sci. 39 (2014) 683–706.

[2] C. Ribeiro, C.M. Costa, D.M. Correia, J. Nunes-Pereira, J. Oliveira, P. Martins, R. Gonçalves, V.F. Cardoso, S. Lanceros-Méndez, Electroactive poly(vinylidene fluoride)-based structures for advanced applications, Nat. Protoc. 13 (2018) 681–704.

[3] R.E. Prud'homme, Crystallization and morphology of ultrathin films of homopolymers and polymer blends, Prog. Polym. Sci. 54–55 (2016) 214–231.

[4] Z. Cui, N.T. Hassankiadeh, Y. Zhuang, E. Drioli, Y.M. Lee, Crystalline polymorphism in poly(vinylidenefluoride) membranes, Prog. Polym. Sci. 51 (2015) 94–126.

[5] H. Kawai, The Piezoelectricity of Poly (vinylidene Fluoride), Jpn. J. Appl. Phys. 8 (1969) 975–976.

[6] V. Sencadas, R. Gregorio, S. Lanceros-Méndez, α to β phase transformation and microestructural changes of PVDF films induced by uniaxial stretch, J. Macromol. Sci. Part B Phys. 48 (2009) 514–525.

[7] S. Satapathy, S. Pawar, P.K. Gupta, K.B. RVarma, Effect of annealing on phase transition in poly(vinylidene fluoride) films prepared using polar solvent, Bull. Mater. Sci. 34 (2011) 727–733.

[8] Y. Jiang, Y. Ye, J. Yu, Z. Wu, W. Li, J. Xu, G. Xie, Study of thermally poled and corona charged poly(vinylidene fluoride) films, Polym. Eng. Sci. 47 (2007) 1344–1350.

[9] P. Costa, J. Silva, V. Sencadas, C.M. Costa, F.W.J. van Hattum, J.G. Rocha, S. Lanceros-Mendez, The effect of fibre concentration on the α to β-phase transformation, degree of crystallinity and electrical properties of vapour grown carbon nanofibre/poly(vinylidene fluoride) composites, Carbon 47 (2009) 2590–2599.

[10] P. Martins, C.M. Costa, M. Benelmekki, G. Botelho, S. Lanceros-Mendez, On the origin of the electroactive poly(vinylidene fluoride) β-phase nucleation by ferrite nanoparticles via surface electrostatic interactions, CrystEngComm. 14 (2012) 2807–2811.

[11] J. Martín, D. Zhao, T. Lenz, I. Katsouras, D.M. de Leeuw, N. Stingelin, Solid-state-

processing of δ-PVDF, Mater. Horizons. 4 (2017) 408–414.

[12] A.C. Lopes, C.M. Costa, C.J. Tavares, I.C. Neves, S. Lanceros-Mendez, Nucleation of the Electroactive γ Phase and Enhancement of the Optical Transparency in Low Filler Content Poly(vinylidene)/Clay Nanocomposites, J. Phys. Chem. C. 115 (2011) 18076–18082.

[13] Y. Ahn, J.Y. Lim, S.M. Hong, J. Lee, J. Ha, H.J. Choi, Y. Seo, Enhanced piezoelectric properties of electrospun poly(vinylidene fluoride)/multiwalled carbon nanotube composites due to high β-phase formation in poly(vinylidene fluoride), J. Phys. Chem. C. 117 (2013) 11791–11799.

[14] N. Jia, Q. Xing, G. Xia, J. Sun, R. Song, W. Huang, Enhanced β-crystalline phase in poly(vinylidene fluoride) films by polydopamine-coated BaTiO3 nanoparticles, Mater. Lett. 139 (2015) 212–215.

[15] Y. Xin, X. Qi, H. Tian, C. Guo, X. Li, J. Lin, C. Wang, Full-fiber piezoelectric sensor by straight PVDF/nanoclay nanofibers, Mater. Lett. 164 (2016) 136–139.

[16] J. Chen, D. Wu, K.C. Tam, K. Pan, Z. Zheng, Effect of surface modification of cellulose nanocrystal on nonisothermal crystallization of poly(β-hydroxybutyrate) composites, Carbohydr. Polym. 157 (2017) 1821–1829.

[17] D.G. Gray, Transcrystallization of polypropylene at cellulose nanocrystal surfaces, Cellulose 15 (2008) 297–301.

[18] S. Kashani Rahimi, R. Aeinehvand, K. Kim, J.U. Otaigbe, Structure and Biocompatibility of Bioabsorbable Nanocomposites of Aliphatic-Aromatic Copolyester and Cellulose Nanocrystals, Biomacromolecules. 18 (2017) 2179–2194.

[19] E. Lizundia, J.L. Vilas, L.M. León, Crystallization, structural relaxation and thermal degradation in Poly(l-lactide)/cellulose nanocrystal renewable nanocomposites., Carbohydr. Polym. 123 (2015) 256-265.

[20] A. Dufresne, Nanocellulose: A new ageless bionanomaterial, Mater. Today. 16 (2013) 220–227.

[21] E. Lizundia, U. Goikuria, J.L. Vilas, F. Cristofaro, G. Bruni, E. Fortunati, I. Armentano, L. Visai, L. Torre, Metal nanoparticles embedded in cellulose nanocrystal based films: material properties and post-use analysis, Biomacromolecules 19 (2018) 2618-2628.

[22] C. Zhou, R. Chu, R. Wu, Q. Wu, Electrospun polyethylene oxide/cellulose nanocrystal composite nanofibrous mats with homogeneous and heterogeneous

microstructures, Biomacromolecules. 12 (2011) 2617–2625.

[23] E. Lizundia, M. Delgado-Aguilar, P. Mutje, E. Fernandez, B. Robles-Hernandez, M.R. de la Fuente, J.L. Vilas, L.M. Leon, Cu-coated cellulose nanopaper for green and low-cost electronics, Cellulose 23 (2016) 1997–2010.

[24] M.-B. Myrian Silva, Pamela Molina, V.V. Aldás, Biopolymers based on polylactic acid and starch: an alternative for the preservation of the environment, DYNA 93 (2017) 581.

[25] J. Kim, S. Yun, Z. Ounaies, Discovery of cellulose as a smart material, Macromolecules. 39 (2006) 4202–4206.

[26] F. Kollmann, V. A. Bazhenov: Piezoelectric Properties of Wood (Authorized Translation from the Russian). Consultants Bureau, New York 1961. 180 S., 4°, 55 Abb. Preis: $ 9.50, Zeitschrift Für Elektrochemie, Berichte Der Bunsengesellschaft Für Phys. Chemie. 66 (n.d.) 522–523.

[27] L. Csoka, I.C. Hoeger, O.J. Rojas, I. Peszlen, J.J. Pawlak, P.N. Peralta, Piezoelectric effect of cellulose nanocrystals thin films, ACS Macro Lett. 1 (2012) 867–870.

[28] S. Bodkhe, P.S.M. Rajesh, S. Kamle, V. Verma, Beta-phase enhancement in polyvinylidene fluoride through filler addition: Comparing cellulose with carbon nanotubes and clay, J. Polym. Res. 21 (2014).

[29] F. Ejaz Ahmed, B.S. Lalia, N. Hilal, R. Hashaikeh, Underwater superoleophobic cellulose/electrospun PVDF–HFP membranes for efficient oil/water separation, Desalination. 344 (2014) 48–54.

[30] B.S. Lalia, E. Guillen, H.A. Arafat, R. Hashaikeh, Nanocrystalline cellulose reinforced PVDF-HFP membranes for membrane distillation application, Desalination. 332 (2014) 134–141.

[31] A.A. Issa, M. Al-Maadeed, A.S. Luyt, M. Mrlik, M.K. Hassan, Investigation of the physico-mechanical properties of electrospun PVDF/cellulose (nano)fibers, J. Appl. Polym. Sci. 133 (2016).

[32] I. Filpponen, D.S. Argyropoulos, Regular Linking of Cellulose Nanocrystals via Click Chemistry: Synthesis and Formation of Cellulose Nanoplatelet Gels, Biomacromolecules 11 (2010) 1060–1066.

[33] D. Liu, T. Zhong, P.R. Chang, K. Li, Q. Wu, Starch composites reinforced by bamboo cellulosic crystals, Bioresour. Technol. 101 (2010) 2529–2536.

[34] M. Roman, W.T. Winter, Effect of sulfate groups from sulfuric acid hydrolysis on

the thermal degradation behavior of bacterial cellulose, Biomacromolecules 5 (2004) 1671–1677.

[35] V. Sencadas, R. Gregorio Filho, S. Lanceros-Mendez, Processing and characterization of a novel nonporous poly(vinilidene fluoride) films in the β phase, J. Non. Cryst. Solids. 352 (2006) 2226–2229.

[36] T. Kondo, C. Sawatari, A Fourier transform infra-red spectroscopic analysis of the character of hydrogen bonds in amorphous cellulose, Polymer 37 (1996) 393–399.

[37] X. Colom, F. Carrillo, Crystallinity changes in lyocell and viscose-type fibres by caustic treatment, Eur. Polym. J. 38 (2002) 2225–2230.

[38] N. Lin, C. Bruzzese, A. Dufresne, TEMPO-oxidized nanocellulose participating as crosslinking aid for alginate-based sponges, ACS Appl. Mater. Interfaces. 4 (2012) 4948–4959.

[39] P. Lu, Y. Lo Hsieh, Cellulose isolation and core-shell nanostructures of cellulose nanocrystals from chardonnay grape skins, Carbohydr. Polym. 87 (2012) 2546–2553.

[40] E. Lizundia, E. Fortunati, F. Dominici, J. L. Vilas, L. M, Leon, I. Armentano, L. Torre, J. M. Kenny, PLLA-grafted cellulose nanocrystals: role of the CNC content and grafting on the PLA bionanocomposite film properties, Carbohydr. Polym. 142 (2016) 105-113.

[41] E. Lizundia, T. D. Nguyen, J.L. Vilas, W.Y. Hamad, M.J. MacLachlan, Chiroptical, morphological and conducting properties of chiral nematic mesoporous cellulose/polypyrrole composite films, J. Mater. Chem. A. 5 (2017) 19184-19194.

[42] J. Kressler, R. Schafer, R. Thomann, Imaging of Semicrystalline Polymers and Polymer Blends by FT-IR Microspectroscopy, Appl. Spectrosc. 52 (1998) 1269–1273.

[43] L. Wang, Y. Wang, Z. Huang, Y. Weng, Heat resistance, crystallization behavior, and mechanical properties of polylactide/nucleating agent composites, Mater. Des. 66 (2015) 7–15.

[44] E. Lizundia, A. Oleaga, A. Salazar, J.R. Sarasua, Nano- and microstructural effects on thermal properties of poly (l-lactide)/multi-wall carbon nanotube composites, Polymer 53 (2012) 2412–2421.

[45] E. Lizundia, L. Perez-Alvarez, M. Saenz-Perez, D. Patrocinio, J. L. Vilas, Physical aging and mechanical performance of Poly (L-lactide)/ZnO nanocomposites, J. Appl. Polym. Sci. 133 (2016) 43619.

[46] S. Hietala, M. Koel, E. Skou, M. Elomaa, F. Sundholm, Thermal stability of styrene grafted and sulfonated proton conducting membranes based on poly(vinylidene fluoride), J. Mater. Chem. 8 (1998) 1127–1132.

[47] E.L. U. Goikuria, A. Larrañaga, J. L. Vilas, Thermal stability increase in metallic nanoparticles-loaded cellulose nanocrystal nanocomposites, Carbohydr. Polym. 171 (2017) 193-201.

[48] X. Ni, W. Cheng, S. Huan, D. Wang, G. Han, Electrospun cellulose nanocrystals/poly(methyl methacrylate) composite nanofibers: Morphology, thermal and mechanical properties, Carbohydr. Polym. 206 (2019) 29–37.

[49] J.M. Raquez, Y. Habibi, M. Murariu, P. Dubois, Polylactide (PLA)-based nanocomposites, Prog. Polym. Sci. 38 (2013) 1504–1542.

[50] C. Carfagna, V. Ambrogi, R. Avolio, P. Cerruti, M.E. Errico, G. Gentile, G. Nasti, Polymer nanocomposites: functionalisation of the nanofiller and control of the interface, Adv. Mater. Process. Technol. 1 (2015) 423–434.

[51] W. Ma, J. Zhang, X. Wang, S. Wang, Effect of PMMA on crystallization behavior and hydrophilicity of poly(vinylidene fluoride)/poly(methyl methacrylate) blend prepared in semi-dilute solutions, Appl. Surf. Sci. 253 (2007) 8377–8388.

[52] E. Lizundia, T.D. Nguyen, J.L. Vilas, W.Y. Hamad, M.J. MacLachlan, Chiroptical luminescent nanostructured cellulose films, Mater. Chem. Front. 1 (2017) 979-987.

[53] G. Cheng, M. Zhou, Y.J. Wei, F. Cheng, P.X. Zhu, Comparison of mechanical reinforcement effects of cellulose nanocrystal, cellulose nanofiber, and microfibrillated cellulose in starch composites, Polym. Compos. 40 (2018) E365-E372.

[54] N. Domun, H. Hadavinia, T. Zhang, T. Sainsbury, G.H. Liaghat, S. Vahid, Improving the fracture toughness and the strength of epoxy using nanomaterials – a review of the current status, Nanoscale. 7 (2015) 10294–10329.

[55] X. Cao, Y. Habibi, L.A. Lucia, One-pot polymerization, surface grafting, and processing of waterborne polyurethane-cellulose nanocrystal nanocomposites, J. Mater. Chem. 19 (2009) 7137–7145.

[56] J.C.H. Affdl, J.L. Kardos, The Halpin-Tsai equations: A review, Polym. Eng. Sci. 16 (1976) 344–352.

[57] W.J. Lee, A.J. Clancy, E. Kontturi, A. Bismarck, M.S.P. Shaffer, Strong and stiff: High-performance cellulose nanocrystal/poly(vinyl alcohol) composite fibers, ACS Appl. Mater. Interfaces. 8 (2016) 31500–31504.

[58] R. Rusli, S.J. Eichhorn, Determination of the stiffness of cellulose nanowhiskers and the fiber-matrix interface in a nanocomposite using Raman spectroscopy, Appl. Phys. Lett. 93 (2008)..

[59] N.V. Reddy, C.R. Kumar, V.V.R.N. Rao, Dielectric properties of amorphous cellulose acetate-butyrate polymer films, Polym. Int. 32 (1993) 381–384.

[60] E. Lizundia, A. Maceiras, J.L. Vilas, P. Martins, S. Lanceros-Mendez, Magnetic cellulose nanocrystal nanocomposites for the development of green functional materials, Carbohydr. Polym. 175 (2017) 425–432.

[61] L. Li, M. Yu, C. Jia, J. Liu, Y. Lv, Y. Liu, Y. Zhou, C. Liu, Z. Shao, Cellulosic Biomass-Reinforced Polyvinylidene Fluoride Separators with Enhanced Dielectric Properties and Thermal Tolerance, ACS Appl. Mater. Interfaces. 9 (2017) 20885–20894.

[62] Y. Chen, S. Zhang, X. Liu, Q. Pei, J. Qian, Q. Zhuang, Z. Han, Preparation of solution-processable reduced graphene oxide/polybenzoxazole nanocomposites with improved dielectric properties, Macromolecules. 48 (2015) 365–372.

[63] J.Y. Kim, T. Kim, J.W. Suk, H. Chou, J.H. Jang, J.H. Lee, I.N. Kholmanov, D. Akinwande, R.S. Ruoff, Enhanced dielectric performance in polymer composite films with carbon nanotube-reduced graphene oxide hybrid filler, Small. 10 (2014) 3405–3411.

[64] C. Jia, Z. Shao, H. Fan, R. Feng, F. Wang, W. Wang, J. Wang, D. Zhang, Y. Lv, Barium titanate as a filler for improving the dielectric property of cyanoethyl cellulose/antimony tin oxide nanocomposite films, Compos. Part A Appl. Sci. Manuf. 86 (2016) 1–8.

[65] A.K. Jonscher, The “universal” dielectric response, Nature. 267 (1977) 673-379.

[66] A. Ladhar, M. Arous, H. Kaddami, M. Raihane, A. Kallel, M.P.F. Graça, L.C. Costa, Ionic hopping conductivity in potential batteries separator based on natural rubber–nanocellulose green nanocomposites, J. Mol. Liq. 211 (2015) 792–802.

[67] A.M. Abdel-karim, A.H. Salama, M.L. Hassan, Electrical conductivity and dielectric properties of nanofibrillated cellulose thin films from bagasse, J. Phys. Org. Chem. 31 (2018) e3851.

Supplementary data

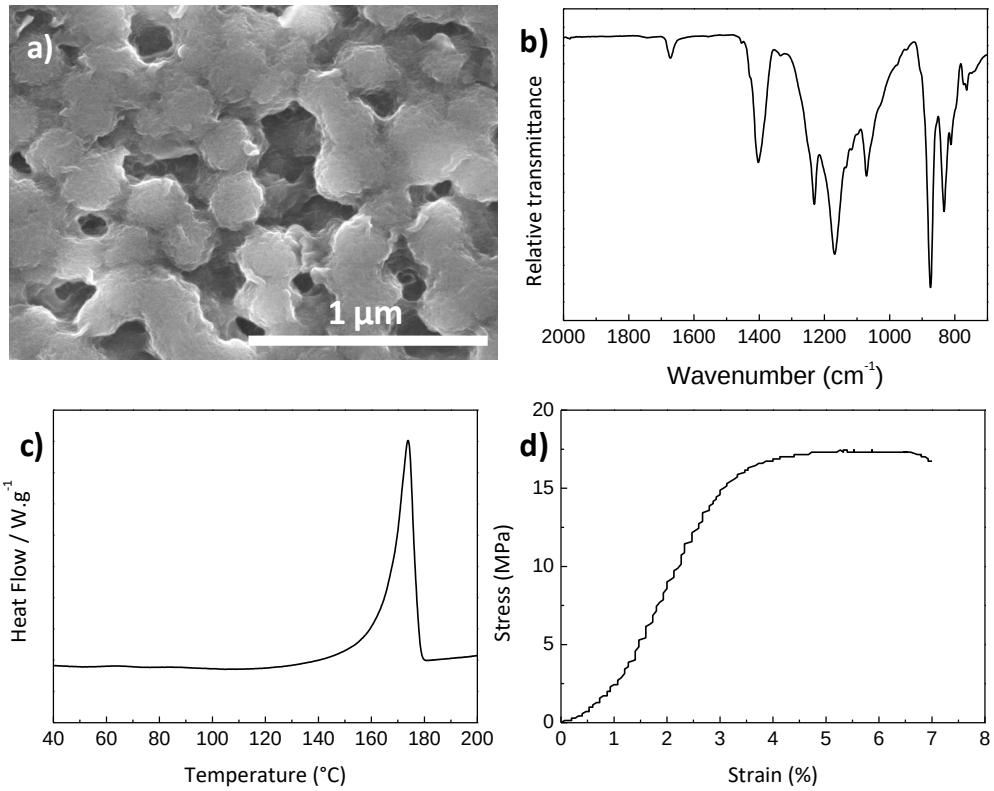

Fig. S1. (a) Representative SEM image; (b) FTIR spectra; (c) DSC heating scan and (d) stress-strain tensile curve for PVDF obtained upon drying at 60 °C at atmospheric pressure.

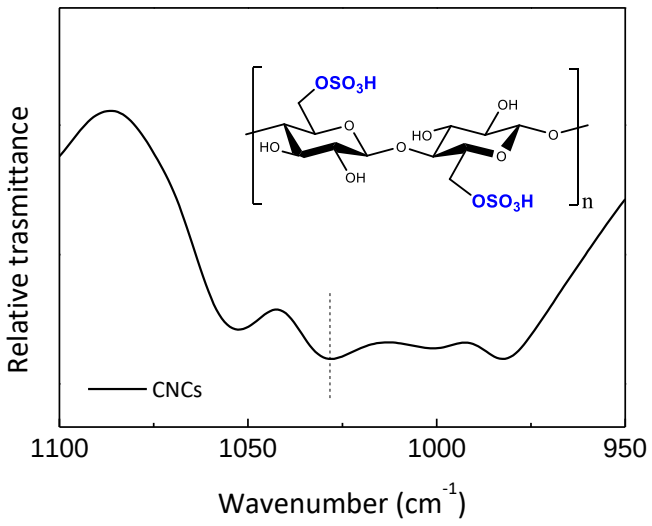

Fig. S2. Enlarged FTIR spectrum highlighting the band located at 1033 cm^{-1} corresponding to sulphate half-ester groups in CNCs.